nature portfolio

https://doi.org/10.1038/s41550-022-01632-z

Supplementary information

Discovery of high-frequency retrograde vorticity waves in the Sun

In the format provided by the authors and unedited

Supplementary Information: Discovery of high-frequency retrograde vorticity waves in the Sun

Chris S. Hanson,[1] Shravan Hanasoge,[2,1*] and Katepalli R. Sreenivasan[1,3]

[1]Center for Space Science, New York University Abu Dhabi, UAE
[2]Department of Astronomy and Astrophysics, Tata Institute of Fundamental Research, Mumbai, India
[3]New York University, New York, USA

*To whom correspondence should be addressed; E-mail: hanasoge@tifr.res.in.

S1 Notations

The radial vorticity in the ring-diagram and LCT horizontal flow maps is evaluated through

$$\eta(r,\theta,\phi,t) = \frac{1}{R_\odot \sin\theta}\left(\frac{\partial}{\partial\theta}(v_x \sin\theta) + \frac{\partial v_y}{\partial\phi}\right), \tag{1}$$

where v_x and v_y are the horizontal flows, measured in small patches on the solar disk, aligned in the direction of rotation and the solar north pole, respectively. $R_\odot$ denotes the radius of the Sun.

Spherical harmonic transforms are then computed via

$$\eta_{\ell m}(r,t) = \int_\pi^0 \int_0^{2\pi} \eta(r,\theta,\phi,t) Y_\ell^m(\theta,\phi) \sin\theta \, \mathrm{d}\phi \, \mathrm{d}\theta, \tag{2}$$

where

$$Y_\ell^m = \sqrt{\frac{(2\ell+1)}{4\pi}\frac{(\ell-m)!}{(\ell+m)!}} P_\ell^m(\cos\theta) e^{im\phi}. \tag{3}$$

The temporal Fourier transform of a function $f(t)$ of observation length T is computed through

$$f(\omega) = \frac{1}{\sqrt{T}} \sum_t f(t) e^{i\omega t}, \tag{4}$$

where ω is the angular frequency.

S1.1 Regime description

For clarity in the regimes discussed in this paper we provide an overview here.

The waves that are used by helioseismic techniques to probe large-scale flows, e.g. acoustic and surface-gravity modes, propagate with frequencies on the order of millihertz. For the best signal-to-noise, waves with frequencies between 2 and 5 mHz are typically used. These waves propagate in an acoustic cavity, trapped between the surface and some depth governed by the mode's wave number and the stratification of the star. The propagation of waves in the Sun is well understood, and differences between the observed waves and those of theory give insight into the unknown subsurface motions of the sun.

Inertial waves, such as the Rossby and HFR modes discussed here, have their restoring force as the Coriolis force. As such, they propagate with frequencies of the order of the Sun's equatorial rotation rate $\Omega = 421.41$ nHz, with spatial scales comparable to the radius of the Sun. These waves are typically described by spherical harmonics (Eq. 2). Inertial waves induce motions in the fluid, which alters the aforementioned acoustic wave propagation. Observing the changes in the acoustic waves allows determination of the inertial wave motion. Figure S1 shows a schematic of the surface motions of the inertial waves discussed in this paper.

S2 Slices of the power spectra

Figure S2 shows slices of the vorticity spectrum, at different ℓ. The datasets include HMI and GONG mode-coupling and ring-diagram vorticity maps, as well as HMI LCT. The observation period is the same for all data sets, from May 2010 to January 2020. These ℓ have the greatest

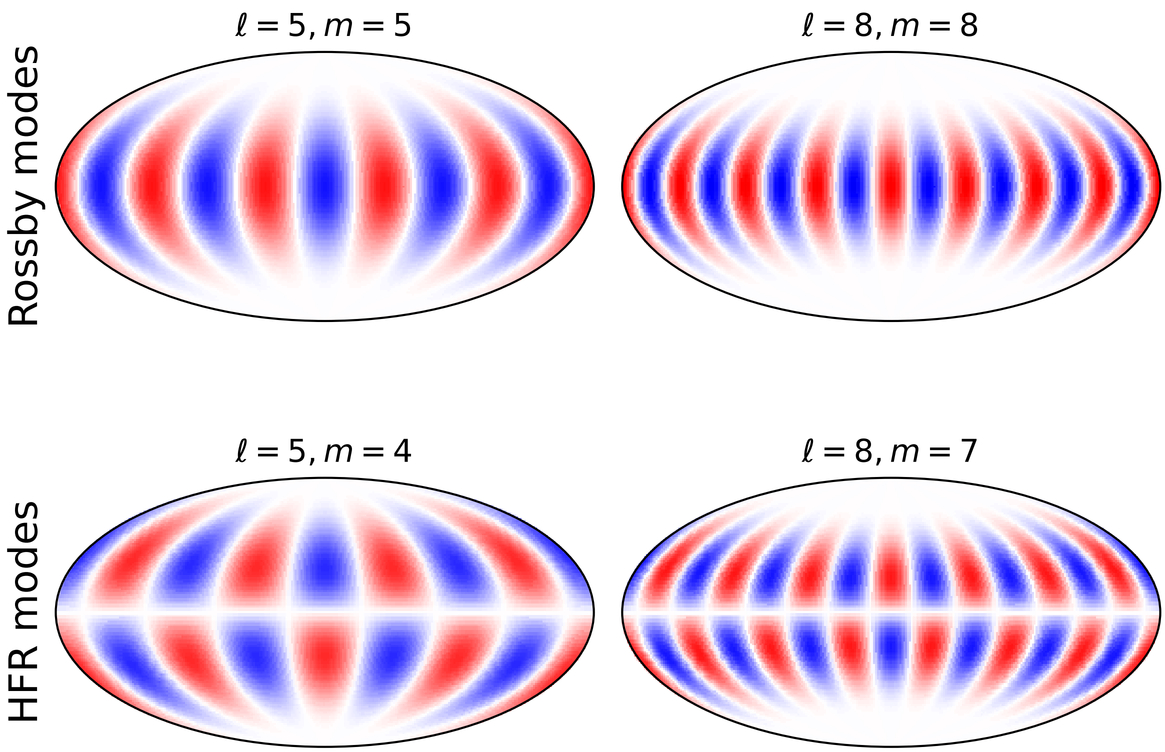

Figure S1: **Schematic of the Rossby and the HFR waves.** Schematic of the surface vortical motions of Rossby waves (top) and HFR waves (bottom) for $\ell = 5, 8$ (left and right, respectively). Clockwise vortical motion is shown as red and anticlockwise as blue. Both waves peak near the equator, however, Rossby modes are symmetric with respect to the equator, while HFR modes are antisymmetric.

signal-to-noise ratio for Lorentzian fitting.

S3 Leakage of power

Due to the partial coverage of the solar disk, there is an apparent replication of spectral features. This repetition is called leakage and results in power being split across frequencies and spherical harmonics. Power from channel m and centered at frequency ω leaks into the $m \pm 1$ channel at frequency $\omega \mp 421.41$ nHz, with reduced amplitude. Here, these leaked signals are referred to as the side lobes of the true power spectral features. In the analysis of Rossby modes, the observed leakage has been modelled (*1, 2*), and we follow this analysis in the context of HFR modes.

S3.1 Leakage from prograde activity

In some prior studies, flows associated with active regions have been mistakenly interpreted as arising from large-scale convection or as signatures of thermal-Rossby modes (*3, 4*). Given that both active-region vorticities and HFR modes are anti-symmetric across the equator, we investigate (and discard) the possibility that the HFR modes are actually leaked prograde activity into the retrograde. Figure S3 shows the prograde and retrograde branches of the smoothed power spectra in Fig. 1.

While the side lobe is seen in the prograde frequencies in the ring-diagram and LCT data, it is absent in the coupling spectrum. The coupling analysis has side lobes every 2×421.41 nHz, for reasons that have been described (*5*).

Qualitatively, the retrograde branches in the ring-diagram and LCT are stronger in amplitude than the prograde branches (Fig. S3 A-E). To quantify this, in Fig. S3F we integrate the power within two line widths of the central frequencies of the HFR modes and compare the ratio between the retrograde signal and prograde side lobe. We find that, in the GONG ring-diagrams

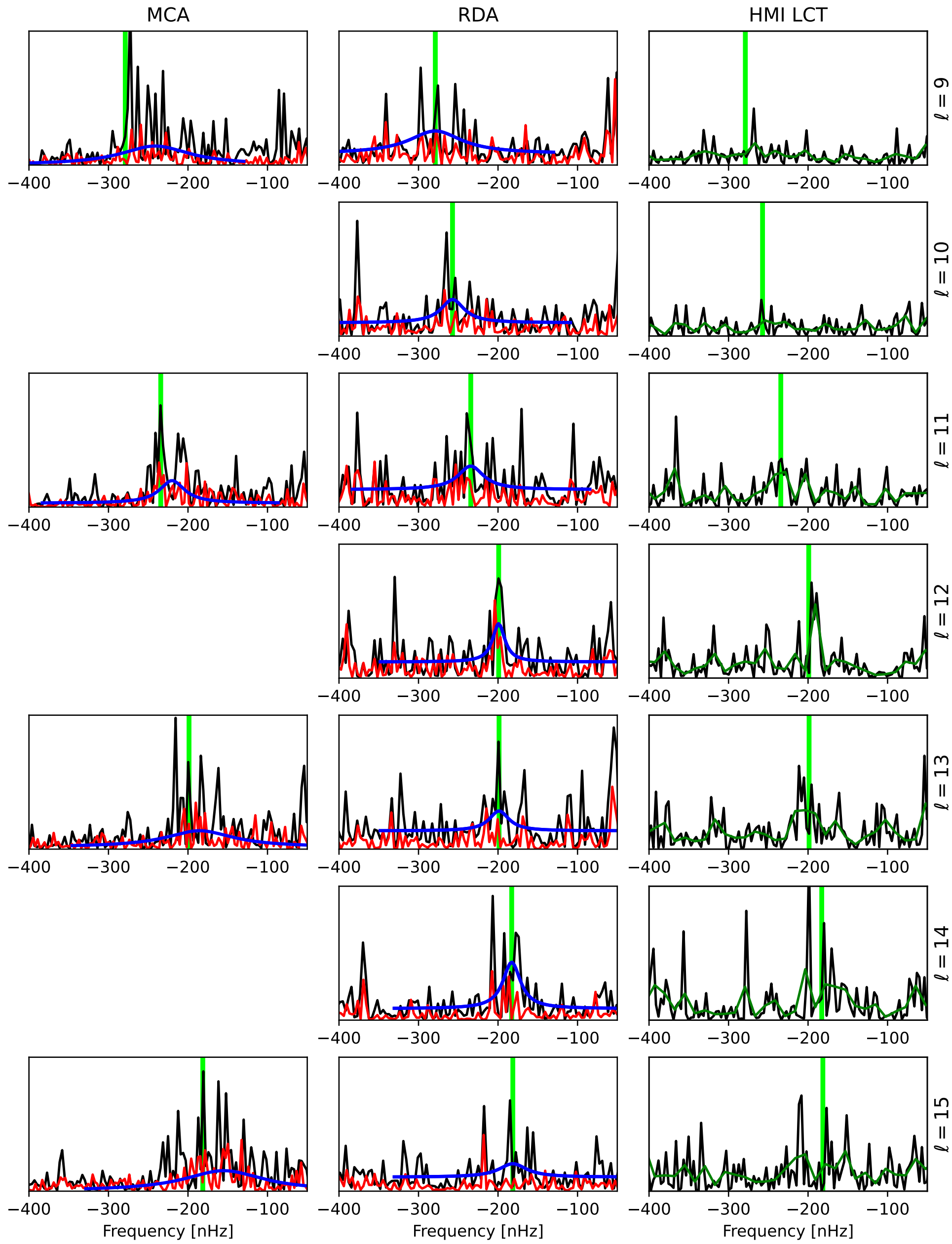

Figure S2: **Vorticity power spectra slices of the high-frequency retrograde vorticity waves.** Slices of the unsmoothed vorticity power spectrum, observed from 2010-2020, for mode coupling (left column), ring-diagrams (middle column) and HMI LCT (right column) from $\ell = 9$ to $\ell = 15$ (top to bottom rows). Negative frequencies indicate retrograde motion. Data from the HMI instrument are shown in black and data from GONG are in red. Due to the poor signal in the LCT data, we have overplotted the smoothed spectra (dark green). The resonant frequencies from the HMI RDA fits are demarcated by vertical light-green lines. The Lorentzian fits for the HMI mode-coupling and HMI ring-diagram spectra are shown in the respective columns (blue) for the range over which the fit was performed.

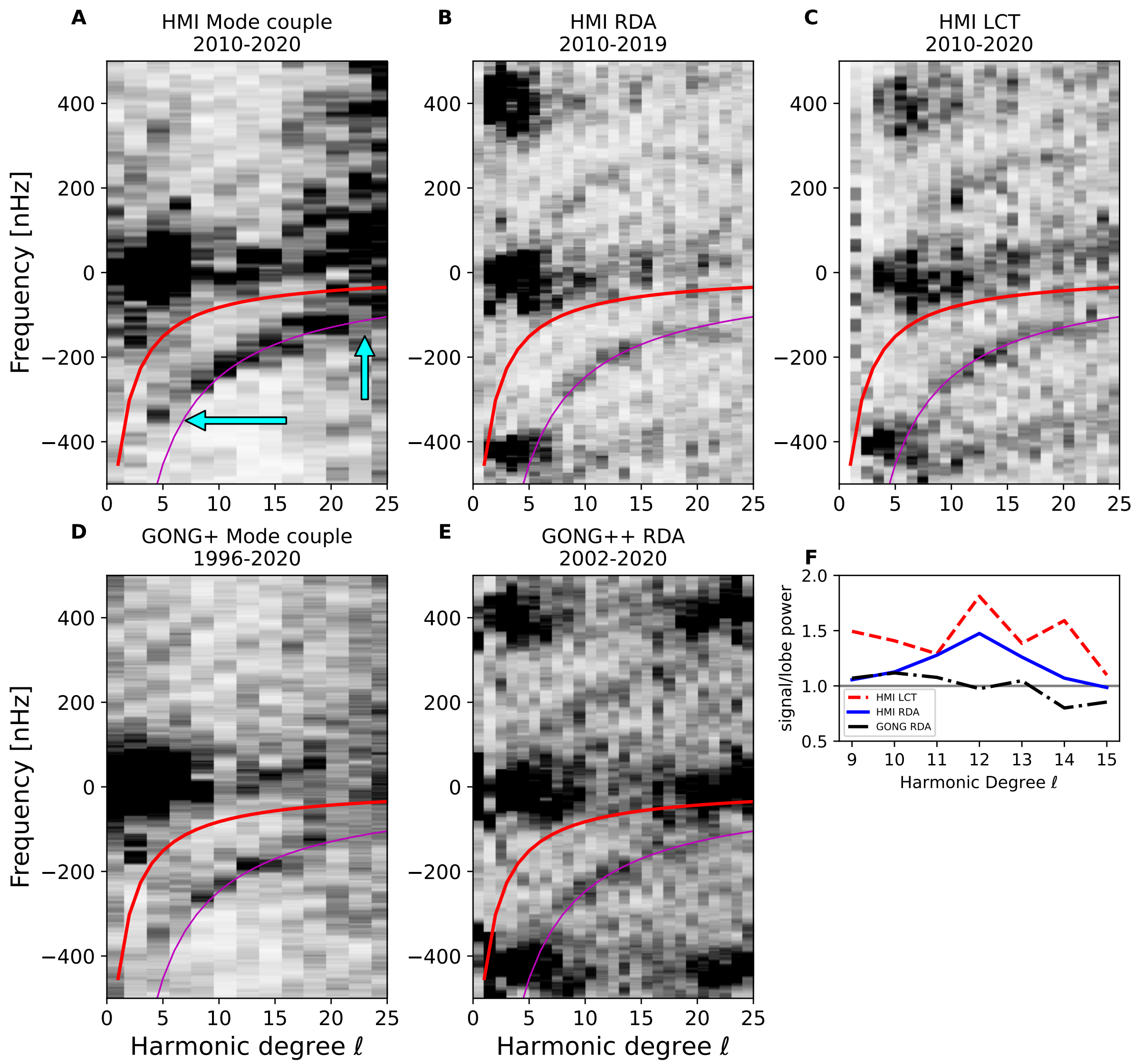

Figure S3: **Spectral leakage due to partial observations of the sun's surface.**.Panels A-E are the same as Fig. 1, except showing prograde (positive) and retrograde (negative) frequencies, with a smoothing window function ~ 30 nHz wide. In the mode-coupling spectra (left panels), the power associated with activity is seen in the prograde frequencies but the HFR mode is only visible in the retrograde (magenta line, between the cyan arrows). The ring-diagram and LCT spectra contain side lobes in the prograde frequencies with reduced amplitudes. Panel F shows the ratio between the integrated power, within two line widths of the central frequency, of the retrograde signal and the prograde side lobe. HMI LCT, HMI and GONG ring-diagrams are shown by the red dashed, blue solid and black dot-dash lines, respectively.

the prograde and retrograde power are too similar to be conclusive. However, in the HMI ring-diagrams and LCT, the retrograde branch shows a power excess of up to 50% greater than the prograde side lobe. This suggests that the retrograde ridge is the true signal. Beyond $\ell = 15$ the ring-diagram analysis and LCT cannot discriminate which branch is the true signal.

The mode-coupling (both HMI and GONG) and the HMI rings and LCT data support the argument that the HFR ridge is retrograde. This inference, taken together with the positive group speed, allows the conclusion that the HFR ridge is not due to the flows associated with active regions.

S4 Spherical Harmonic components

Fig. S4 shows the different spherical-harmonic components of the Rossby and HFR modes from the HMI data. Because the Rossby and HFR modes are not exactly described by spherical harmonics, some power is seen in neighbouring azimuthal orders. For instance, in the case of Rossby modes the power is seen in the $\ell = m$ and (weakly) $\ell = m + 2$ channels. The same is true for the HFR modes, with the signal seen in $\ell = m + 1$ and weakly in the $\ell = m + 3$ channels. At higher values of $\ell - m$, no signal is observed above the noise.

S5 Depth Dependence

Figure S5 shows the HMI ring-diagram spectra for three different depths. The methods used here are sensitive to the upper few percent of the solar convection zone. The HMI ring-diagram pipeline computes flow maps at 31 different depths from $R_\odot$ down to $0.97R_\odot$. Here, we average three sets of 10 spectra, corresponding to three depths, and plot the unsmoothed spectra. We neglect spurious flow maps at the surface $R_\odot$ (*6*). The HFR ridge is clearly seen at all ring-diagram analysis depths, though the signal-to-noise ratio becomes small with depth. Future studies will need to determine the radial eigenfunction of the HFR modes at greater depths, and

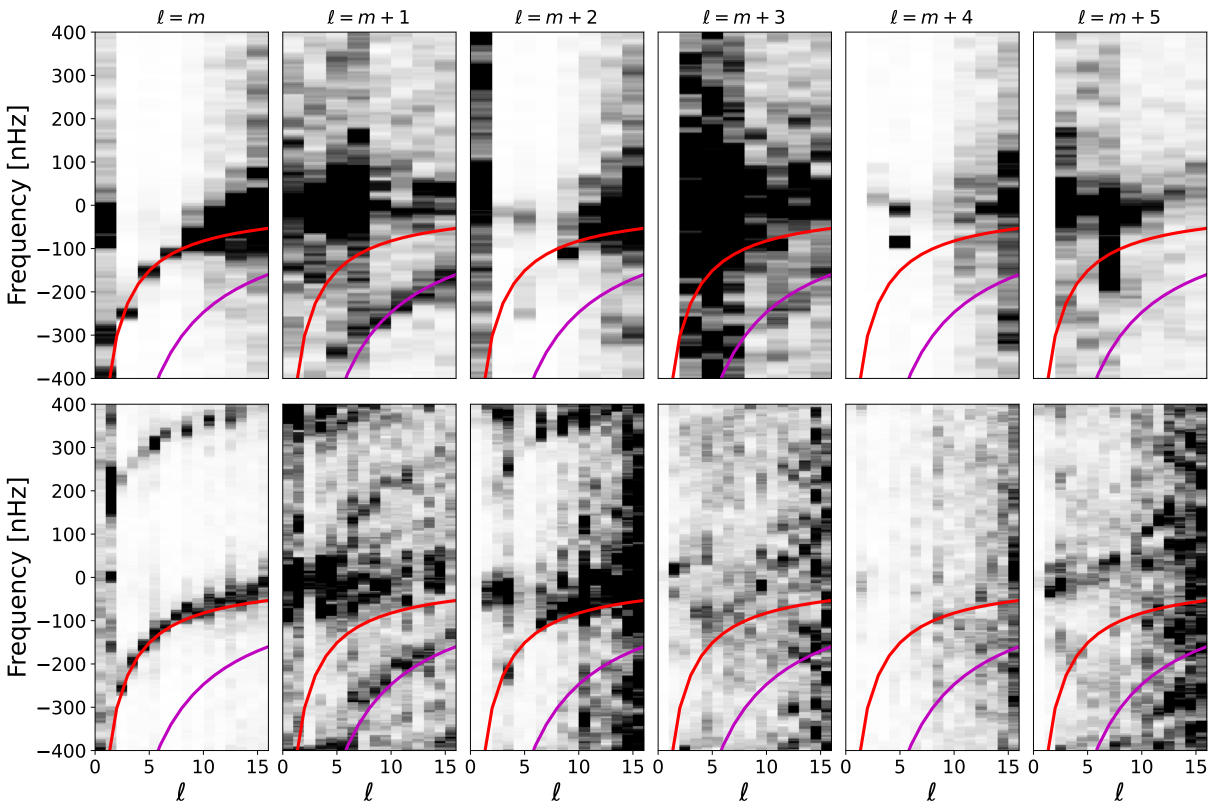

Figure S4: **Spherical harmonic components of the Rossby and HFR waves.** Top row: HMI mode-coupling spectra for different values of $\ell - m$ (see column titles). Bottom row: HMI Ring-diagram spectra for the same $\ell - m$ values as in the corresponding upper panels. Negative frequencies indicate retrograde motion. Each ℓ is scaled by the maximum value of the spectrum between -400 and 100 nHz. Color scales where $\ell - m$ is even are determined by twice the maximum values of the $\ell = m$ spectra, while the odd $\ell - m$ are scaled by twice the maximum values in the $\ell - m = 1$ spectra. The red line shows the theoretical dispersion of Rossby modes, while the magenta line highlights the approximate HFR dispersion.

compare them to the Rossby modes (which have yet to be measured themselves).

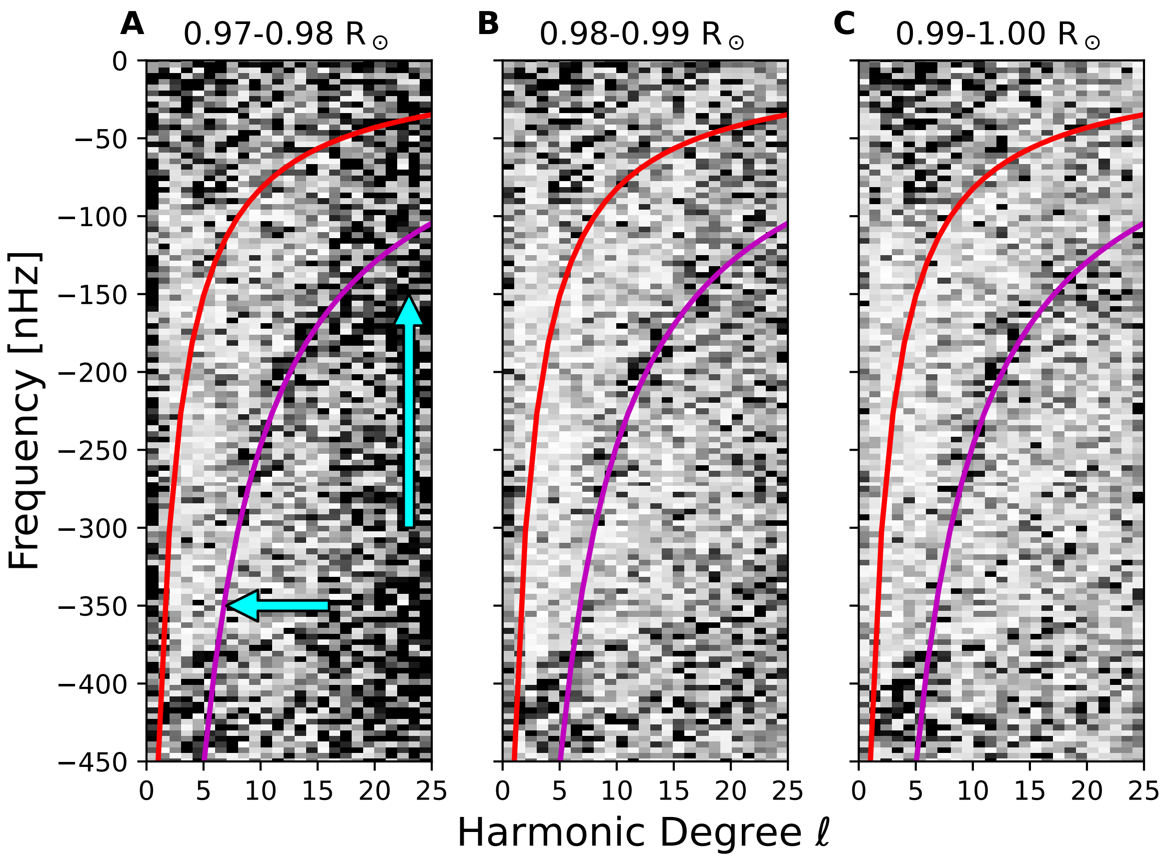

Figure S5: **Depth dependence of the HFR waves.** The $\ell = m + 1$ HMI ring-diagram radial vorticity power spectrum for different depths. The HMI ring-diagram pipeline computes flows at 30 depths from 0.97R$_\odot$ to R$_\odot$. We average three sets of 10 spectra to determine the panels. The HFR modes are seen to depths of 3% of the solar radius. All panels are normalized in the same manner as Fig. 1. The color scale is normalized to the power in panel (**C**). The red line shows the theoretical dispersion of Rossby modes, the magenta line shows the approximate HFR dispersion, while the cyan arrows highlights the extent of the ridge of power identified as HFR modes.

S6 Divergence

Figure S6 shows the HMI ring-diagram horizontal divergence spectra in the symmetric $\ell = m$ channel. Panel A shows the presence of weak divergence signal in the retrograde frequencies.

However, this power does not coincide with the measured dispersion relation in the vorticity. Panel B and C show slices of the power spectra and the shifted power from prograde frequencies (421.41 nHz away). Due to partial observational coverage of the solar disk, signals are repeated every 421.41 nHz, with each repetition being smaller in amplitude than the original. While panel B shows that the retrograde vorticity signal is of greater amplitude than the prograde (hence the true signal), panel C shows the opposite (prograde greater than retrograde). This suggests that the retrograde divergence signal is a replication of the prograde divergence signal, possibly arising from large scale active region inflow patterns (*7*).

Mode coupling analysis does not appear to suffer from the replication at every 421.41 nHz. Analysis of the HMI mode-coupling sound speed spectra (which, like the divergence, is also indicative of thermal phenomena) reveals some signal in the $\ell = m = 12$ channel in the same frequency bins as that of the corresponding HFR mode. Signal in all other ℓ is absent. These pixels are above the 95% confidence level for the background noise (i.e. 95% of pixels are expected below). However, given that this is not supported by ring-diagram analysis, LCT, GONG+ coupling, or in other m, we cannot conclude that this feature is associated with HFR phenomena.

S7 Fitting routines

The HFR and Rossby wave power spectra P, at a specific ℓ and as a function of frequency ω, may be approximated by a Lorentzian of the form

$$\mathcal{L}_\ell(\omega, \boldsymbol{\lambda}) = \frac{A}{1 + (\omega - \omega_0)^2/(\Gamma/2)^2} + B, \tag{5}$$

where A is the mode amplitude, ω_0 is the mode frequency, Γ is the full width at half maximum, B is the background noise of the spectrum and $\boldsymbol{\lambda} = \{A, \omega_0, \Gamma, B\}$. Estimates of parameters $\boldsymbol{\lambda}$

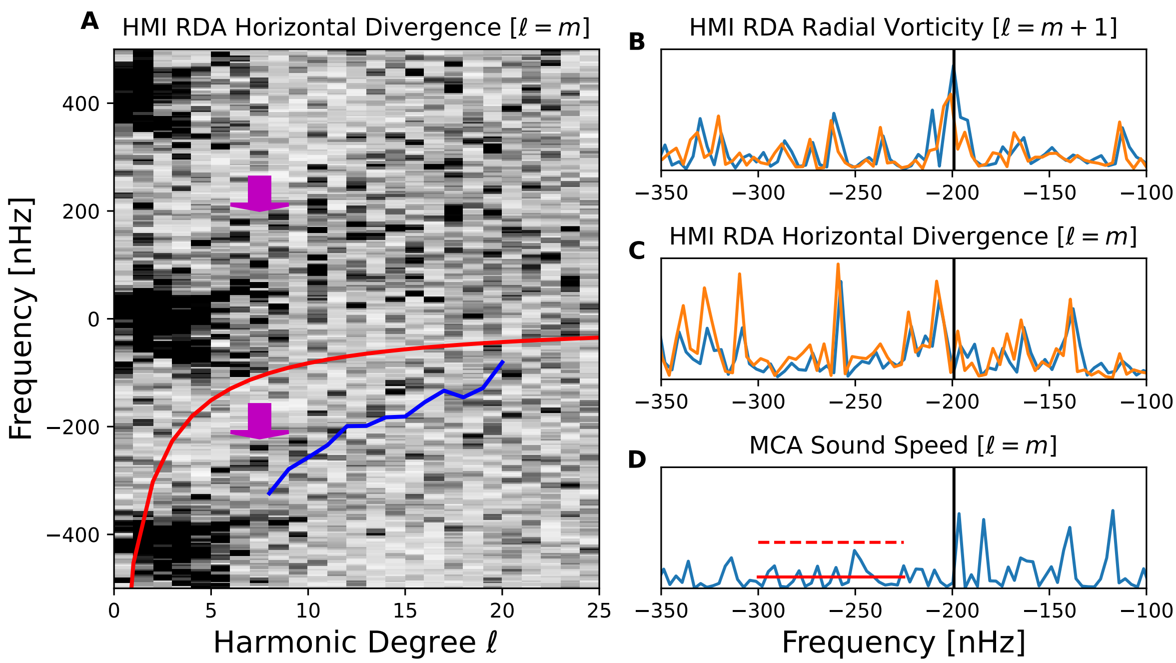

Figure S6: **Divergence spectrum in the frequency and spatial range of HFR waves.** (**A**) Smoothed spectra of the HMI ring-diagram horizontal divergence for $\ell = m$. The purple arrows show the presence of divergence signal in both prograde and retrograde directions, which, however, do not coincide with the measured dispersion relation of HFR waves (blue line). (**B**) Slice of the radial vorticity in the anti-symmetric channel (blue) for $\ell = 12$. Over plotted (orange) is the same spectrum shifted from the prograde frequencies by 421.41 nHz. The retrograde signal is greater than the replication in the prograde direction. (**C**) Same as panel B, except for the symmetric horizontal divergence. In this case, the prograde signal is greater, indicating that the retrograde signal is the replication. (**D**) Slice of the HMI coupling sound-speed spectra. The measured background noise is shown by the solid red line. The 95% confidence level (where 95% of pixels are expected to be below) is shown by the dashed red line. In panels B-D the measured HFR mode frequency is shown by the black vertical line.

in Eq. 5 are determined by minimizing the negative of the log-likelihood function,

$$J_\ell(\boldsymbol{\lambda}_\ell) = \sum_{k=1}^{K} \ln \mathcal{L}_\ell(\omega_k, \boldsymbol{\lambda}) + P(\ell, \omega_k)/\mathcal{L}_\ell(\omega_k, \boldsymbol{\lambda}), \tag{6}$$

where ω_k is the k-th frequency bin within a frequency window consisting of K frequencies.

The minimization of J_ℓ and the estimates on the fitting errors were computed from samples drawn by Markov chain Monte Carlo (MCMC) methods. Priors on the frequencies are $\omega_0 \in [3\Omega_m^{\mathrm{RH}} - 150\ \mathrm{nHz}, 3\Omega_m^{\mathrm{RH}} + 150\ \mathrm{nHz}]$, where Ω_m^{RH} is theoretical dispersion relation of Rossby-Haurwitz modes at azimuthal order m. Priors on A and B are chosen such that the MCMC samples were drawn from the set $[0, 5 \times \max P(\ell, \omega)]$. The prior on the line width is $\Gamma \in [2(\omega_{k+1} - \omega_k), 200\ \mathrm{nHz}]$. We utilized the python library emcee (*8*) with 100 walkers and 1000 steps. The first 200 steps were taken as burn-in, and we computed the 16$^{\text{th}}$, 50$^{\text{th}}$, and 84$^{\text{th}}$ percentiles from the remaining 800 steps. We verified these results with the semi-analytical method in (*9*). The results obtained through MCMC are presented here since the error calculations are more numerically stable.

In cases where Lorentzian fits are poor due to weak signal-to-noise A/B, we use spectral centroids to estimate the central frequency. The central frequency is estimated through

$$\omega_0 = \frac{\sum_{k=1}^{K} \omega_k P(\ell, \omega_k)}{\sum_{k=1}^{K} P(\ell, \omega_k)} \tag{7}$$

where the window in frequency is 40 nHz wide centered on the approximate peak of the smoothed spectra.

In addition to the ring-diagram mode fits in Table 1, Table S1 shows the mode fit parameters for the HMI mode-coupling data set.

ℓ	m	Frequency (nHz)	Frequency Ratio	Line width (nHz)	Line width Ratio	signal-to-noise	Amplitude Ratio %
5	4	$-329.0^{15.2}_{11.8}$	$2.0^{0.1}_{0.1}$	$83.1^{77.9}_{60.3}$	$7.3^{8.0}_{5.9}$	3.2	$1.7^{0.1}_{0.0}$
7	6	-	-	-	-	-	-
9	8	$-241.2^{9.5}_{8.2}$	$2.6^{0.1}_{0.1}$	$106.3^{29.1}_{26.8}$	$4.1^{1.9}_{1.5}$	103.4	$7.4^{0.6}_{0.3}$
11	10	$-220.1^{6.8}_{6.6}$	$2.8^{0.2}_{0.2}$	$38.2^{26.7}_{14.7}$	$0.7^{0.6}_{0.3}$	5.8	$13.5^{1.3}_{0.7}$
13	12	$-185.5^{10.1}_{10.4}$	$3.2^{0.4}_{0.4}$	$103.3^{49.2}_{56.0}$	$1.9^{1.1}_{1.1}$	8.3	$24.5^{4.3}_{2.8}$
15	14	$-155.1^{9.5}_{9.3}$	$2.4^{0.2}_{0.2}$	$121.7^{32.5}_{30.1}$	$2.5^{1.0}_{0.9}$	133.7	$26.2^{4.8}_{2.8}$

Table S1: Mode fit parameters of the HFR vorticity waves from fits to the HMI coupling power spectra. Ratios between HFR and Rossby mode frequencies, line widths and amplitudes are also provided. The superscripts and subscripts are the estimated upper and lower bounds of the 1 sigma error, respectively. The signal-to-noise ratio is the ratio between the mode amplitude and the background noise level. There is no clear $\ell = 7$ mode above the noise, and hence been ommitted here.

S8 Equatorial symmetries of vorticity and Reynolds stresses

Since the divergence associated with both HFR and Rossby modes is zero, the vorticity, which is given by,

$$\eta = \frac{1}{r \sin\theta}\left[\frac{\partial(v_\phi \sin\theta)}{\partial\theta} - \frac{\partial v_\theta}{\partial\phi}\right], \tag{8}$$

alone dictates the symmetries of the velocity field. Firstly, we note that taking the derivative results in a flipping of symmetries, i.e., for an equatorially symmetric longitudinal velocity $v_\phi \sin\theta$ (note that $\sin\theta$ is symmetric), $\partial_\theta(v_\phi \sin\theta)$ is anti-symmetric. Thus, to obtain anti-symmetric η, we will require v_ϕ to be symmetric and v_θ to be anti-symmetric. The Reynolds stresses, $\langle v_\phi v_\theta \rangle$ are therefore anti-symmetric. Thus, for HFR modes, v_ϕ is symmetric and v_θ, η and Reynolds stresses are anti-symmetric. Similarly, it can be argued that, for the observed Rossby modes, η and v_ϕ have to be symmetric, and v_θ and Reynolds stresses are anti-symmetric.

S9 Eigenvalue solver

Assuming the observed modes are magnetized and that they manifest solely in radial vorticity and have zero radial velocity component (i.e., they are divergence free), they would likely be excited in a convectively stable layer. The super-adiabatic near-surface layers show significant radial motions, and are unlikely to be the location where these waves are generated (although we do not have evidence to rule that scenario out). The base of the convection zone is a much more plausible region in this context, with hydrodynamic Rossby waves propagating through toroidal magnetic fields, resulting in an altered dispersion relation and enhanced phase speeds. The hydrodynamic component of these motions would need to penetrate up to the surface. The shape of the associated dispersion relation has much to teach us about the field configuration and amplitude at the base of the convection zone, two critical inputs to dynamo theory.

The eigenvalue equation for shallow-water MHD is given by (omitting differential rotation)

$$\begin{aligned} 0 =& \frac{\omega^2}{m^2}\left[\frac{d}{d\mu}\left\{(1-\mu^2)\frac{d}{d\mu}\right\} - \frac{m^2}{(1-\mu^2)}\right]\Psi - \frac{2\Omega_0\omega}{m}\Psi \\ & - B\left[\frac{d}{d\mu}\left\{(1-\mu^2)\frac{d}{d\mu}\right\} - \frac{m^2}{(1-\mu^2)}\right](B\Psi) + B\Psi\frac{d^2(B(1-\mu^2))}{d\mu^2}, \end{aligned} \tag{9}$$

where $B(\theta)$ is a toroidal magnetic field and θ is co-latitude, $\mu = \cos\theta$, Ω_0 the solid-body rotation rate, ω the eigenfrequency and $\Psi(\theta)$ the eigenfunction. Because the problem is linear, we decompose the problem into separate and independent problems for each azimuthal order m. We project the eigenfunctions on to the associated Legendre polynomial basis, $P_{\ell m}(\mu)$, which satisfy the following relations

$$\int_{-1}^{1} d\mu\, P_{\ell m}P_{km} = \delta_{k,\ell}, \tag{10}$$

and

$$\left\{\frac{d}{d\mu}\left[(1-\mu^2)\frac{d}{d\mu}\right] - \frac{m^2}{(1-\mu^2)}\right\}P_{\ell m}(\mu) = -\ell(\ell+1)P_{\ell m}. \tag{11}$$

Note that the eigenfunctions are given by individual polynomials only for very specific field configurations; for general fields, the eigenfunctions can depart notably from the associated Legendre polynomials. For fixed m, we adopt the following ansatz

$$\Psi = \sum_q \alpha_q P_{qm}, \quad B\Psi = \sum_k \beta_k P_{km}. \tag{12}$$

We can linearly transform $B\Psi$ to Ψ using the following matrix relation

$$\int d\mu P_{\ell m}(\mu)\, B\, \Psi = \beta_\ell = \sum_q \alpha_q \int d\mu B\, P_{\ell m}\, P_{qm} = \sum_q T_{\ell q}\alpha_q \tag{13}$$

and obtain

$$\{\beta\} = T\{\alpha\}, \quad T_{\ell q} = \int d\mu B\, P_{\ell m}\, P_{qm}, \tag{14}$$

where $\{\alpha\}$ is the column vector denoting the contributions of different associated Legendre polynomials to the eigenfunction. Thus, equation (9), when used in conjunction with the orthogonality relation (10) and the polynomial differential equation (11), reduces to

$$-\sum_q \left[\frac{\omega^2}{m^2}q(q+1) - \frac{2\Omega_0\omega}{m}\right]\alpha_q P_{qm} = \sum_k \{(k(k+1)\beta_k - d_\mu^2[B(1-\mu^2)]\,\alpha_k\}\, B(\mu)\, P_{km}, \tag{15}$$

where, for brevity's sake, we denote $d_\mu = d/d\mu$. Multiplying by $P_{\ell m}(\mu)$ and integrating both sides with respect to μ, we obtain

$$\begin{aligned}\sum_q \delta_{\ell,q}\left[\frac{2\Omega_0\omega}{m} - \frac{\omega^2}{m^2}q(q+1)\right]\alpha_q = \sum_k k(k+1)\Big\{T_{kk'}\int d\mu P_{km}P_{\ell m}B \\ -\delta_{k,k'}\int d\mu P_{km}P_{\ell m}B d_\mu^2[B(1-\mu^2)]\Big\}\,\alpha_{k'},\end{aligned} \tag{16}$$

where the two integrals are written as matrices, one of which was already defined in equation (13). This can be shown to simplify to a straightforward matrix eigenvalue equation,

$$A\{\alpha\} = \lambda\{\alpha\}, \tag{17}$$

where λ are the eigenvalues. To numerically solve this equation, we set a maximum harmonic degree $\ell_{\max}$, and since $\ell \geq m$, we obtain $\ell_{\max} - m + 1$ eigenvalues for which m. A critical step is to divide both sides in equation (16) by $\ell(\ell+1)$, which ensures numerical convergence of the eigenvalues. The LHS of equation (16) thus reduces to $[2\Omega_0\omega/m - \omega^2\ell(\ell+1)/m^2]\alpha_\ell$. We verify convergence by changing $\ell_{\max}$ from 50 to 100 in steps of 10, finding, in each case, only minute differences in the eigenvalues.

Figure S7 compares the dispersion relations of the magnetized-Rossby waves with the $\ell = m$ Rossby mode and the HFR waves. The magnetized waves have a clear prograde branch and their frequencies generally increase with wavenumber, both of which contrast with the HFR modes. It is useful here to recall that the usage of harmonic-degree ℓ is not quite right, as described earlier in this section. We use it loosely here to denote the first equatorially symmetric ("$\ell = m$") and anti-symmetric ("$\ell = m+1$") channels.

S9.1 2D differential rotation

We also compute the eigenvalues due to 2D differential rotation and demonstrate that it is too small to be generate HFR waves. The term capturing the departure from solid body rotation (differential rotation) is written as $\Omega_1 = c_2 \sin^2\theta + c_4 \sin^4\theta$; the governing equation for hydrodynamic Rossby waves propagating in a shearing flow $\Omega_0 + \Omega_1$ is given by

$$0 = \left(\Omega_1 - \frac{\omega}{m}\right)^2 \left[\frac{d}{d\mu}\left\{(1-\mu^2)\frac{d}{d\mu}\right\} - \frac{m^2}{(1-\mu^2)}\right]\Psi + 2\Omega_0\left(\Omega_1 - \frac{\omega}{m}\right)\Psi - \left(\Omega_1 - \frac{\omega}{m}\right)\Psi\frac{d^2}{d\mu^2}[\Omega_1(1-\mu^2)]. \quad (18)$$

Substituting the Legendre polynomials and dropping one of the $\Omega_1 - \omega/m$ factors and integrating against $P_{\ell m}$,

$$-\frac{\ell(\ell+1)\omega}{m}\alpha_\ell = \sum_k \left\{2\Omega_0\delta_{k\ell} - \int d\mu P_{km}P_{\ell m}\left(\frac{d^2}{d\mu^2}[\Omega_1(1-\mu^2)] + \Omega_1\right)\right\}\alpha_k. \quad (19)$$

Dividing both sides by $\ell(\ell+1)$ - again, a critical step - we obtain a straightforward matrix eigenvalue problem. The eigenvalues for the $\ell = m+1$ channel, shown in Figure S8, are distinctly different from the HFR modes.

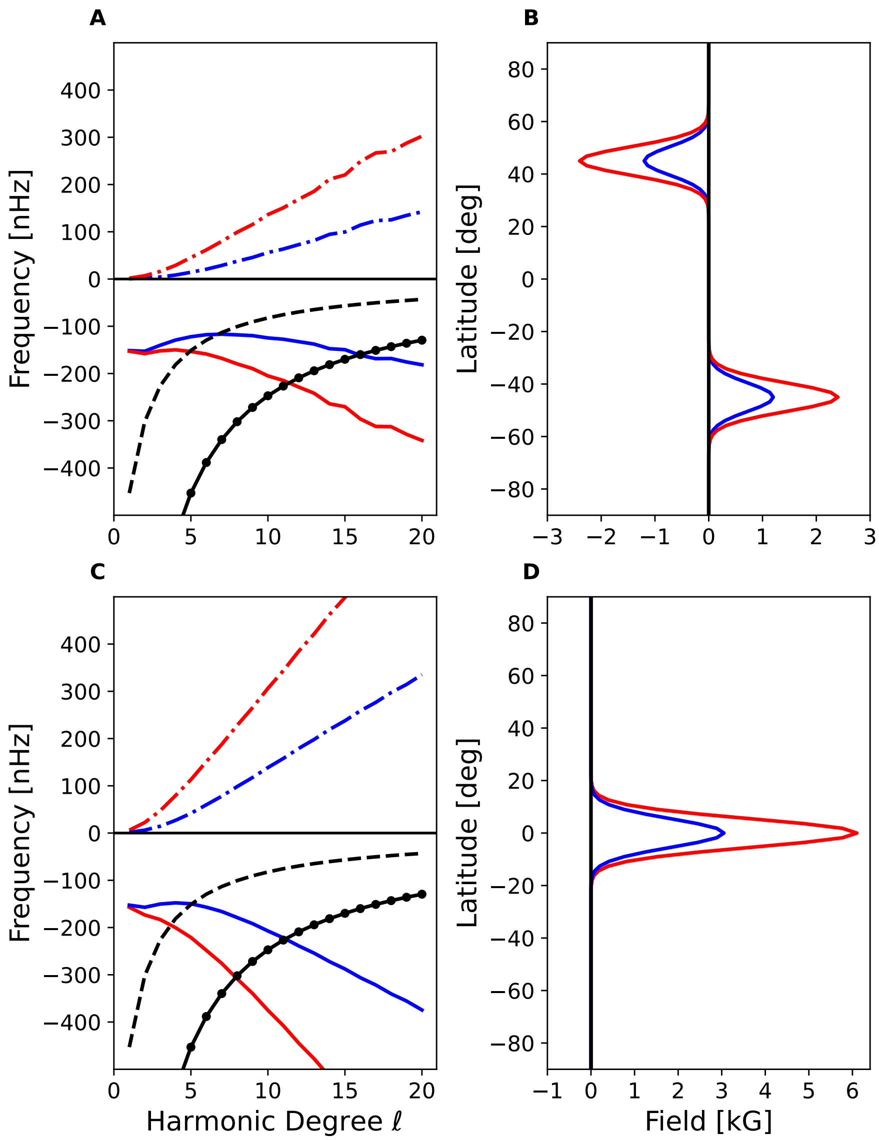

Figure S7: **The dispersion relation of magnetized Rossby waves.** Eigenvalues of the magnetized Rossby wave, shown in panels **A** and **C**, obtained by solving the shallow-water equations with the toroidal fields bands shown in panel **B** and **D**, respectively. The fast retrograde (solid lines) and slow prograde magnetized Rossby waves (dot-dashed) shown in **A** (and **C**) correspond to the field configurations of panel **B** (and **D**), as indicated in blue and red. The sectoral hydrodynamic Rossby mode for $\ell = m$ (black dashed) and the HFR modes (black dot line) are also shown. The field is assumed to be located at the base of the convection zone.

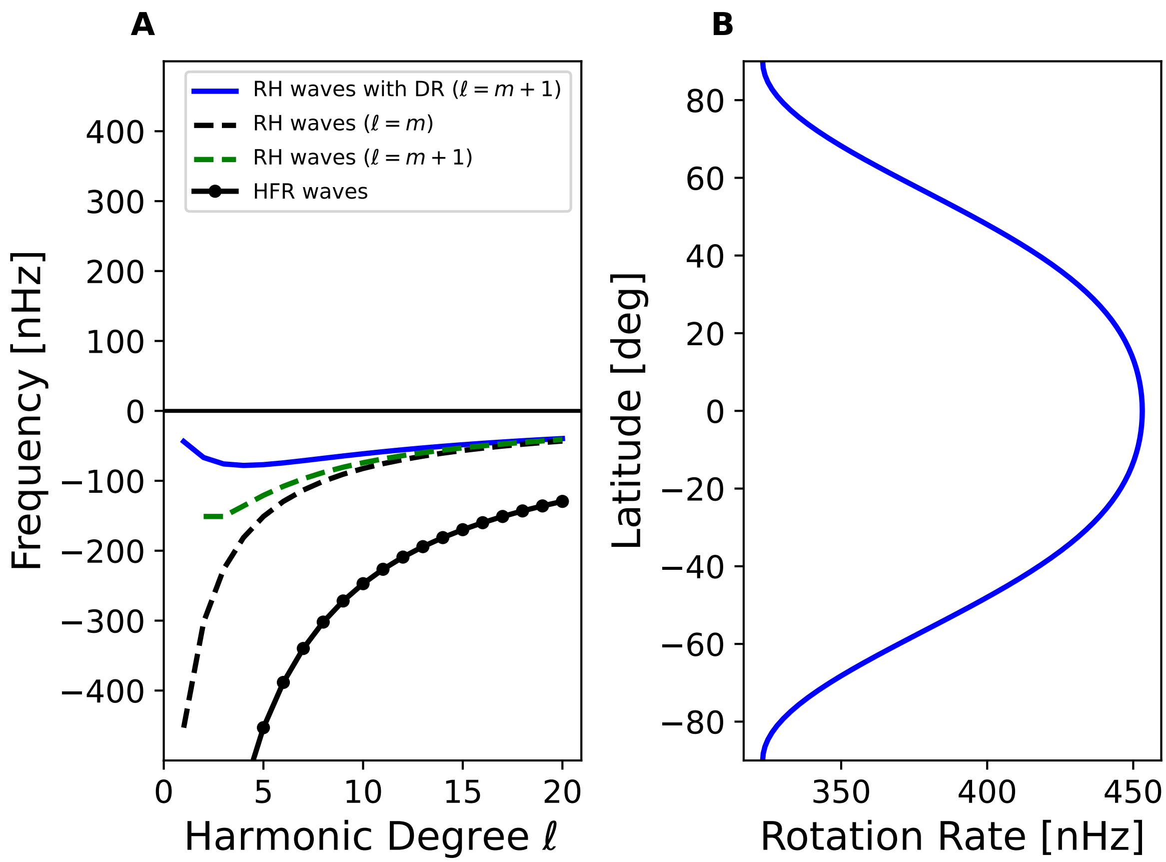

Figure S8: **Dispersion relation of Rossby waves due to latitudinal differential rotation.** Eigenvalues of the $\ell = m + 1$ Rossby wave (blue line, panel **A**), which is altered from the classical Rossby-wave dispersion (green dashed) when latitudinal differential rotation (panel **B**) is present. This is computed using the shallow-water approximation with a 2D profile of rotational shear $\Omega(\theta)/(2\pi) = \left[453.1 - 54.39\sin^2\theta - 75.439\sin^4\theta\right]$ nHz, where θ is co-latitude. Also shown in panel **A** are the HFR modes (black dot-lined) and $\ell = m$ Rossby modes (black dashed).

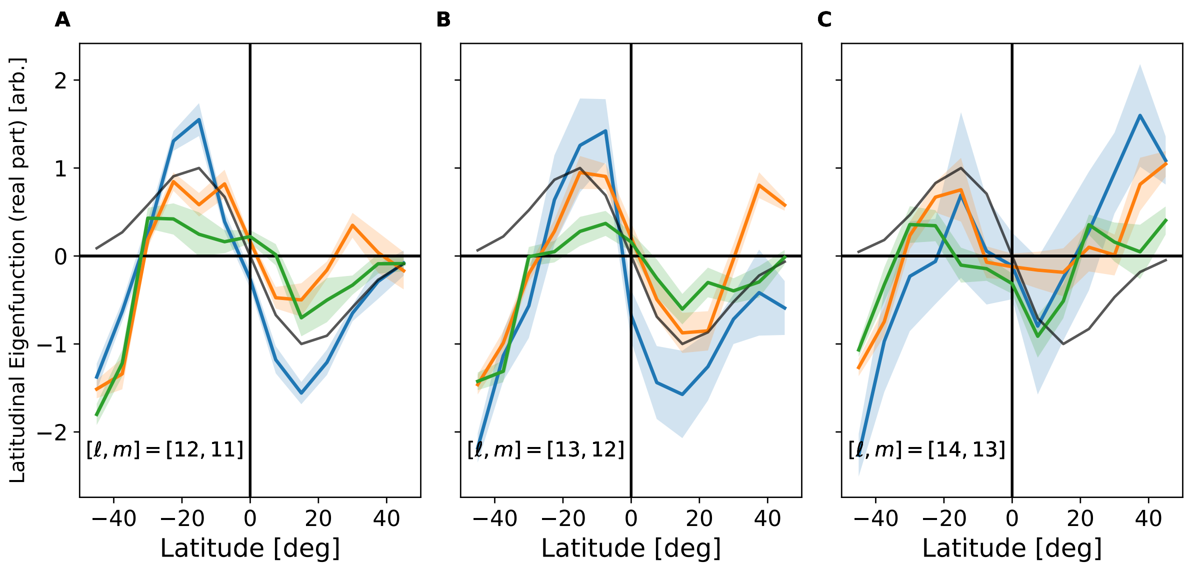

Figure S9: **The latitudinal eigenfunctions of the HFR waves.** The normalized real part of the HFR mode's latitudinal eigenfunction, averaged over all depths down to 20 Mm, for different ℓ from 2010-2020, HMI (blue) and GONG (green), and 2002-2010 GONG (orange), ring-diagram data sets. The shaded region provides an estimate of the scatter in the eigenfunctions, and is calculated from time chunks of $\sim$ 1.25 years. For reference, the corresponding associated Legendre Polynomial is overplotted (grey line).

S10 Latitudinal Eigenfunctions

Figure S9 shows the estimated latitudinal variation of the HFR modes from both the HMI and GONG ring-diagrams. These variations are computed using the singular value decomposition approach outlined in (*6*). We compute the eigenfunctions for depth-averaged flow maps, in chunks of 1.25 years, and estimate the scatter from the variance of the resulting eigenfunctions. We find that the eigenfunctions are antisymmetric, peak in latitude at $\pm$15-20° and change sign at higher latitudes. The latitudinal eigenfunctions are not given by the corresponding associated Legendre polynomials, which is expected in differentially rotating stars (*6*) and explains why the HFR dispersion is seen in $\ell = m + 1, m + 3$.

References and Notes

1. Z.-C. Liang, L. Gizon, A. C. Birch, T. L. Duvall, Time-distance helioseismology of solar Rossby waves. *Astron. Astrophys.* **626**, A3 (2019).

2. C. S. Hanson, L. Gizon, Z.-C. Liang, Solar Rossby waves observed in GONG++ ring-diagram flow maps. *Astron. Astrophys.* **635**, A109 (2020).

3. J. G. Beck, T. L. Duvall, P. H. Scherrer, Long-lived giant cells detected at the surface of the Sun. Nature **394**, 653 (1998).

4. R. K. Ulrich, Very Long Lived Wave Patterns Detected in the Solar Surface Velocity Signal. *Astrophys. J.* **560**, 466 (2001).

5. K. Mandal, S. Hanasoge, Properties of Solar Rossby Waves from Normal Mode Coupling and Characterizing Its Systematics. *Astrophys. J.* **891**, 125 (2020).

6. B. Proxauf, *et al.*, Exploring the latitude and depth dependence of solar rossby waves using ring-diagram analysis. *Astron. Astrophys.* **634**, A44 (2020).

7. C. S. Hanson, T. L. Duvall, A. C. Birch, L. Gizon, K. R. Sreenivasan, Solar east-west flow correlations that persist for months at low latitudes are dominated by active region inflows. *Astron. Astrophys.* **644**, A103 (2020).

8. D. Foreman-Mackey, D. W. Hogg, D. Lang, J. Goodman, emcee: The MCMC Hammer. *Publ. Astron. Soc. Pacific* **125**, 306 (2013).

9. T. Toutain, T. Appourchaux, Maximum likelihood estimators: an application to the estimation of the precision of helioseismic measurements. *Astron. Astrophys.* **289**, 649 (1994).